JOURNAL OF THEORETICAL
AND APPLIED MECHANICS
64, 1, pp. 71–84, Warsaw 2026
https://doi.org/10.15632/jtam-pl/216285

STUDY ON ROOF FRACTURE MECHANISM AND MINE PRESSURE CHARACTERISTICS IN PSEUDO-INCLINED WORKING FACES OF STEEPLY INCLINED COAL SEAMS

Jiadi YIN[1], Yu WU[1*], Yang HAO[1], Kangsheng XUE[1], Yan ZHANG[2], Hualei ZHANG[2]

[1] *State Key Laboratory of Intelligent Construction and Healthy Operation and Maintenance of Deep Underground Engineering, China University of Mining and Technology, Xuzhou, China*
[2] *Anhui University of Science and Technology, Huainan, China*

*corresponding author, *wuyu@cumt.edu.cn*

An improperly designed pseudo-inclination angle in steeply inclined coal seams can lead to coal wall spalling and hydraulic support failure. This study establishes mechanical models for initial and periodic roof fractures under pseudo-inclined mining and derives analytical solutions using the variational method. The optimal pseudo-inclination angle has been determined to be 5° to 10°. Field monitoring shows that initial fractures occur at the center of the working face, while periodic fractures originate in the upper-middle section, where support loads are also highest. These results validate the mechanical model and offer theoretical guidance for the safe mining of steeply inclined seams.

Keywords: steeply inclined coal seam; pseudo-inclined mining; rock layer failure; thin plate model; mining pressure patterns.

1. Introduction

Steeply inclined coal seams are widely distributed in western and central China, accounting for approximately 10 % to 20 % of the country's proven coal reserves (Wu *et al.*, 2020). Due to their large dip angles, these seams exhibit highly complex mining conditions and are recognized as a typical category of difficult-to-mine coal seams (Sun *et al.*, 2019). Under steeply inclined conditions, the downslope component of the gravitational force is enhanced, resulting in significant shear-induced strata sliding. This leads to pronounced asymmetry and unpredictability in roof fracture behavior, ground pressure evolution, and support system stability (Xie *et al.*, 2020). These complex mechanical responses directly influence the effectiveness of roof control, operational safety, and equipment adaptability. Therefore, elucidating the mechanisms governing roof fracture and pressure transmission in steeply inclined coal seams holds considerable theoretical and practical engineering significance.

International research, particularly in the United Kingdom, France, Germany, and Ukraine, began relatively early and focused on the characteristics of stress distribution and ground pressure evolution during mining in steeply inclined seams (Eremin *et al.*, 2022; Das *et al.*, 2017). These studies further promoted the development of fully mechanized mining technologies (Rak *et al.*, 2020; Kumar *et al.*, 2023; Çelik *et al.*, 2023; Das *et al.*, 2021), the design of specialized mining equipment (Proyavkin *et al.*, 1993; Islavath *et al.*, 2016; 2023), and detailed investigations into post-mining strata deformation and surface subsidence (Do *et al.*, 2017). In China, systematic research started in the 1990s and has since supported the transition from non-mechanized to fully mechanized longwall mining (Luo *et al.*, 2021; Tu *et al.*, 2015), resulting in extensive engineering experience and research achievements. Existing studies have revealed the temporal

sequence of roof fracture (Lang *et al.*, 2021), the non-uniformity of goaf filling – an effect that intensifies with an increasing dip angle and the resulting asymmetric deformation patterns and shell-like roof structures (Xie *et al.*, 2020). Ground pressure is particularly severe in the central region of the working face, while the roof weighting intervals vary along the inclination direction (Yang *et al.*, 2020). The asymmetric stress distribution and shear-dominated deformation tendencies predispose hydraulic supports to instability cases, such as sliding, tilting, reverse tilting, and torsion (Li *et al.*, 2017), thus further complicating mining operations. Consequently, flexible shield supports with enhanced anti-slip and anti-shear performance are more suitable for steeply inclined conditions (Zhao *et al.*, 2022), and lateral constraints must be provided during support movement to prevent instability (Wang *et al.*, 2016). To mitigate rock ejection and equipment sliding, a pseudo-inclined face layout has been increasingly adopted in steep seam mining (Pan *et al.*, 2017), resulting in a parallelogram-shaped rather than rectangular roof structure behind the working face. The selection of pseudo-inclination angle plays a critical role in roof control and the stability of the coal wall ahead of the face (Zhang *et al.*, 2025). However, current engineering practices rely mainly on numerical simulations and field experience, lacking a systematic theoretical framework.

In this study, a mechanical model of an elastic thin plate is established for the basic roof of a pseudo-inclined working face in steeply inclined coal seams. The deformation characteristics, principal stress distribution, and the spacing of initial and periodic roof fractures are systematically analyzed, and a rational range of pseudo-inclination angles is proposed. Theoretical results are validated using field monitoring data, providing a transferable theoretical basis and engineering reference for optimizing pseudo-inclined layout, predicting roof weighting behavior, and designing support parameters in steeply inclined coal seam longwall mining.

2. Geological background and technology synopsis

2.1. Geological background

The II4 mining area of the Taoyuan Coal Mine extends approximately 2200 meters along the strike, with a dip width ranging from 900 to 1500 meters, covering an area of about 2.5 km^2. The 1044 working face is located within the no. 10 coal seam in the II4 mining area, as depicted in Fig. 1a. The coal seam thickness varies between 3.2 and 4.2 meters, with a localized parting layer ranging from 0 to 0.23 meters. The coal seam dips at approximately 42°. The immediate roof comprises mudstone and fine sandstone, whereas the floor is predominantly composed of mudstone. The stratigraphic column of the coal seam is presented in Fig. 1b.

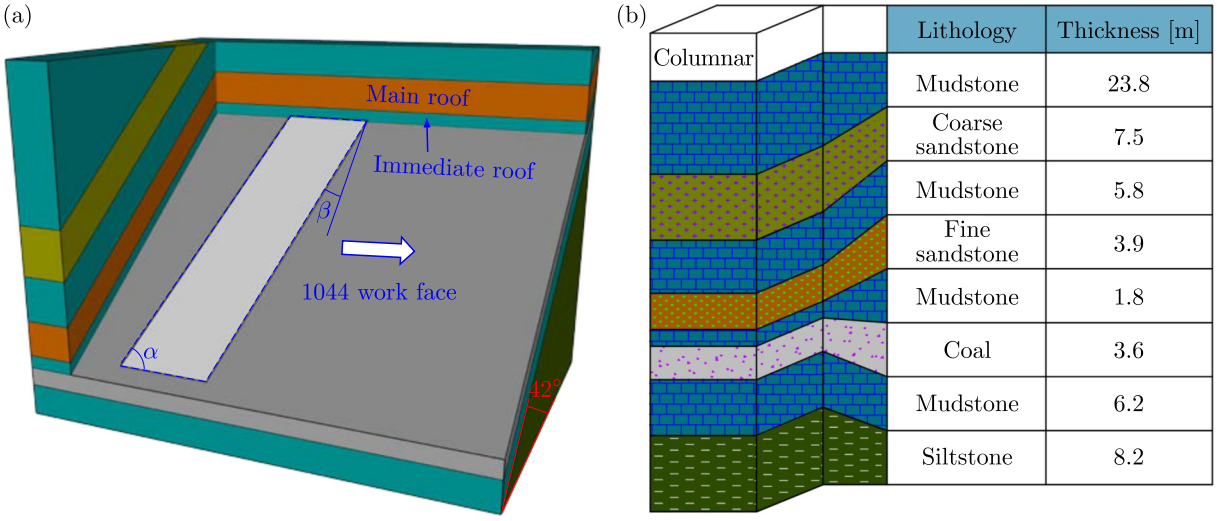

Fig. 1. Geological overview of Coal Mine.

2.2. Technology synopsis

When a steeply inclined working face is arranged along the dip direction of the coal seam, excessive inclination can cause the advancing conveyor and support movement, particularly the pushing of the conveyor to shift downward, creating challenges for coal mining operations (Zhao *et al.*, 2025). The primary issue is that extracted coal tends to slide freely along the coal seam floor, leading to the formation of flying gangue within the entire mining space, which poses significant safety hazards to both equipment and personnel. To address these issues, the 1044 working face adopts a pseudo-inclined layout with an inclination angle of β, as shown in Fig. 1a. This layout offers two key advantages. First, coal naturally slides along the coal wall, reducing potential damage to equipment and minimizing risks to personnel. Second, it leverages the spatial offset between adjacent supports to balance the upward movement caused by support advancement with the downward displacement due to the coal seam inclination, effectively mitigating equipment slippage during the support and conveyor advancement process.

In this working face, the caving method is employed, whereby the goaf is formed as the basic roof and the immediate roof naturally collapses with face advance, producing an accumulation of caved rock. In addition, several engineering measures have been incorporated to enhance equipment stability under mechanized mining conditions on steeply inclined seams. These include anti-slip structures on the bases of hydraulic supports, increased initial supporting force, lateral constraint devices between adjacent supports, and anti-slip control within the shearer traction system, all of which prevent sliding or rolling instability along the dip direction.

3. Mechanical mechanism of main roof fracture

3.1. Mechanical model of the initial fracture

When pseudo-inclined mining is applied to steeply inclined coal seams, as the working face advances, the main roof fails and collapses into the mined-out area, with the roof forming a parallelogram that hangs above the cavity. This leads to periodic deformations and failure. The main roof can be treated as a parallelogram plate for mechanical analysis. Prior to its first fracture, the main roof behaves as an elastically supported thin plate with four fixed edges. The load acting on the inclined plate is considered as the resultant of the normal and tangential forces from the overlying strata. As illustrated in Fig. 2a, the working face has a length of b and an advancement distance of a, with a roof thickness of h. The rock layer exhibits an inclination angle of θ, while the working face is oriented at an angle α relative to the horizontal plane. The pseudo-inclination angle of the working face is β. As shown in Fig. 2b, the boundaries of the working face are constrained on all four sides.

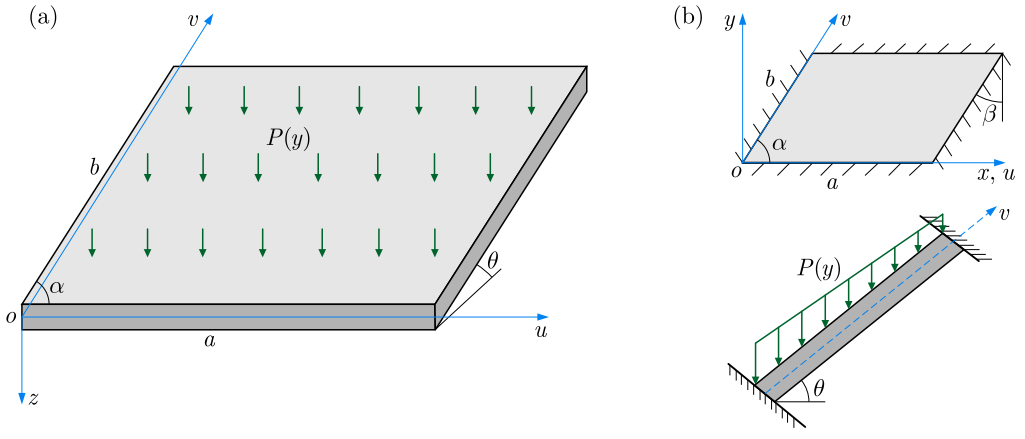

Fig. 2. Mechanical model of initial fracture.

The load function is given by:

$$P(y) = q_0 - ky. \tag{3.1}$$

In the equation, q_0 represents the load applied to the bottom of the main roof, and k is the load distribution coefficient.

The deformation of the parallelogram plate is solved using the Kantorovich approximation method (Wang, 1983). The coordinate transformation is as follows:

$$\begin{cases} u = x - y\cot\alpha, \\ v = y/\sin\alpha. \end{cases} \tag{3.2}$$

Let the deflection function of the roof deformation be denoted as $\omega_1(u, v)$. The strain energy of the main roof can be expressed as

$$U = \frac{D}{2}\iint\limits_S \left(\nabla^2 w_1\right)^2 \mathrm{d}x\,\mathrm{d}y = \frac{D}{2}\iint \frac{1}{\sin^3\alpha}\left[\frac{\partial^2\omega_1}{\partial u^2} - 2\cos\alpha\frac{\partial^2\omega_1}{\partial u\partial v} + \frac{\partial^2\omega_1}{\partial v^2}\right]^2 \mathrm{d}u\,\mathrm{d}v, \tag{3.3}$$

where D is the bending stiffness of the thin plate.

The work done by the load on the main roof is given by

$$W = \iint (q_0 - ky)\cos\theta\omega_1\,\mathrm{d}x\,\mathrm{d}y = \iint (q_0 - kv\sin\alpha)\sin\alpha\cos\theta\omega_1\,\mathrm{d}u\,\mathrm{d}v. \tag{3.4}$$

According to the principle of minimum potential energy, the functional is given by

$$\prod = U - W. \tag{3.5}$$

Let the beam function that satisfies the boundary conditions $v = 0$ and $v = b$ be

$$V = \frac{v^4}{b^4} - 2\frac{v^3}{b^3} + \frac{v^2}{b^2}. \tag{3.6}$$

By solving Eqs. (3.3), (3.4), (3.5), and (3.6) simultaneously, the following results can be obtained:

$$\begin{aligned}\prod = {} & \frac{D}{2}\frac{1}{\sin^3\alpha}\int_0^a \left(\frac{b}{630}U''^2 + \frac{8\cos^2\alpha}{105b}U'^2 + \frac{4}{5b^3}U^2 - \frac{4}{105b}UU''\right)\mathrm{d}u \\ & - \frac{2bq_0 - k\sin\alpha b^2}{60}\sin\alpha\cdot\cos\theta\int_0^a U\,\mathrm{d}u.\end{aligned} \tag{3.7}$$

The following can be derived from the Euler–Lagrange equation:

$$\frac{\partial\prod}{\partial U} - \frac{\mathrm{d}}{\mathrm{d}u}\frac{\partial\prod}{\partial U'} + \frac{\mathrm{d}^2}{\mathrm{d}u^2}\frac{\partial\prod}{\partial U''} = 0. \tag{3.8}$$

By simplifying the calculations, the following ordinary differential equation can be obtained:

$$b^4U'''' - 3(8 + 16\cos^2\alpha)b^2U'' + 504U = (42q_0 - 21k\sin\alpha b)\,b^4\sin^4\alpha\cdot\cos\theta/2/D. \tag{3.9}$$

The general solution of the ordinary differential equation is given by

$$\begin{aligned}U = {} & A_1\cosh\left(\eta\frac{u}{b}\right)\cos\left(\xi\frac{u}{b}\right) + A_2\sinh\left(\eta\frac{u}{b}\right)\sin\left(\xi\frac{u}{b}\right) + A_3\cosh\left(\eta\frac{u}{b}\right)\sin\left(\xi\frac{u}{b}\right) \\ & + A_4\sinh\left(\eta\frac{u}{b}\right)\cos\left(\xi\frac{u}{b}\right) + K.\end{aligned} \tag{3.10}$$

In the equation, $K = (2q_0 - kb\sin\alpha)b^4\sin^4\alpha\cdot\cos\theta/(48D)$, and $\pm(\eta \pm \xi i)$ represent the four roots of the equation $\lambda^4 - 3(8 + 16\cos^2\alpha)\lambda^2 + 504 = 0$.

The deflection function equation of the main roof is given by

$$\omega_1 = UV = \left(\frac{v^4}{b^4} - 2\frac{v^3}{b^3} + \frac{v^2}{b^2}\right)\left[A_1\cosh\left(\eta\frac{u}{b}\right)\cos\left(\xi\frac{u}{b}\right) + A_2\sinh\left(\eta\frac{u}{b}\right)\sin\left(\xi\frac{u}{b}\right) + A_3\cosh\left(\eta\frac{u}{b}\right)\sin\left(\xi\frac{u}{b}\right) + A_4\sinh\left(\eta\frac{u}{b}\right)\cos\left(\xi\frac{u}{b}\right) + A_5\right]. \tag{3.11}$$

The boundary conditions for the initial fracture of the main roof are as follows:

$$\begin{cases} \omega_1|_{v=0,b} = \left.\dfrac{\partial\omega_1}{\partial y}\right|_{v=0,b} = 0, \\ \omega_1|_{u=0,a} = \left.\dfrac{\partial\omega_1}{\partial x}\right|_{u=0,a} = 0. \end{cases} \tag{3.12}$$

By applying the boundary conditions from Eq. (3.12), the following results can be obtained:

$$\begin{cases} A_1 = -K, \\ A_2 = \dfrac{K\left[\cosh\left(\eta\frac{a}{b}\right)\cos\left(\xi\frac{a}{b}\right) - 1\right] + \frac{\eta}{\xi}A_4\cosh\left(\eta\frac{a}{b}\right)\sin\left(\xi\frac{a}{b}\right) - A_4\sinh\left(\eta\frac{a}{b}\right)\cos\left(\xi\frac{a}{b}\right)}{\sinh\left(\eta\frac{a}{b}\right)\sin\left(\xi\frac{a}{b}\right)}, \\ A_3 = -\dfrac{\eta}{\xi}A_4, \\ A_4 = \left\{\begin{array}{l} -\left[\eta\cosh\left(\eta\frac{a}{b}\right)\sin\left(\xi\frac{a}{b}\right) + \xi\cos\left(\xi\frac{a}{b}\right)\sinh\left(\eta\frac{a}{b}\right)\right]K\left[\cosh\left(\eta\frac{a}{b}\right)\cos\left(\xi\frac{a}{b}\right) - 1\right] \\ \quad + \sinh\left(\eta\frac{a}{b}\right)\sin\left(\xi\frac{a}{b}\right)\left[-A_1\eta\sinh\left(\eta\frac{a}{b}\right)\cos\left(\xi\frac{a}{b}\right) + A_1\xi\cosh\left(\eta\frac{a}{b}\right)\sin\left(\xi\frac{a}{b}\right)\right] \end{array}\right\} \Big/ \\ \qquad \left\{\begin{array}{l} \eta\cosh\left(\eta\frac{a}{b}\right)\sin\left(\xi\frac{a}{b}\right)\left[\frac{\eta}{\xi}\cosh\left(\eta\frac{a}{b}\right)\sin\left(\xi\frac{a}{b}\right) - \sinh\left(\eta\frac{a}{b}\right)\cos\left(\xi\frac{a}{b}\right)\right] \\ \quad + \xi\cos\left(\xi\frac{a}{b}\right)\sinh\left(\eta\frac{a}{b}\right)\left[\frac{\eta}{\xi}\cosh\left(\eta\frac{a}{b}\right)\sin\left(\xi\frac{a}{b}\right) - \sinh\left(\eta\frac{a}{b}\right)\cos\left(\xi\frac{a}{b}\right)\right] \\ \quad - \sinh^2\left(\eta\frac{a}{b}\right)\sin^2\left(\xi\frac{a}{b}\right)\left(\frac{\eta^2}{\xi} + \xi\right) \end{array}\right\}. \end{cases} \tag{3.13}$$

3.2. Mechanical model of periodic fracture

During the periodic fracturing stage of the main roof, it remains in a state where three edges are fixed while one edge is suspended. To simplify the boundary conditions, let us refer to Fig. 3.

The solution process for the periodic fracture of the main roof is similar to that of the initial fracture. Let the deflection function for the periodic failure of the main roof be

$$\omega_2(u,v) = U_2V = \left(\frac{v^4}{b^4} - 2\frac{v^3}{b^3} + \frac{v^2}{b^2}\right)U_2. \tag{3.14}$$

Similarly, the calculation for the periodic fracture of the main roof yields:

$$U_2 = B_1\cosh\left(\eta\frac{u}{b}\right)\cos\left(\xi\frac{u}{b}\right) + B_2\sinh\left(\eta\frac{u}{b}\right)\sin\left(\xi\frac{u}{b}\right) + B_3\cosh\left(\eta\frac{u}{b}\right)\sin\left(\xi\frac{u}{b}\right) + B_4\sinh\left(\eta\frac{u}{b}\right)\cos\left(\xi\frac{u}{b}\right) + K. \tag{3.15}$$

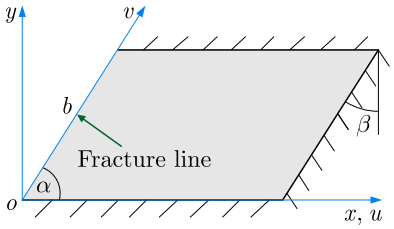

Fig. 3. Mechanical model for the periodic failure.

The boundary conditions for the periodic failure of the main roof are as follows:

$$\begin{cases} \omega_2|_{v=0,b} = \left.\dfrac{\partial \omega_2}{\partial y}\right|_{v=0,b} = 0, \qquad \omega_2|_{u=a} = \left.\dfrac{\partial \omega_2}{\partial x}\right|_{u=a} = 0, \\ M_x|_{u=0} = M_{xy}|_{u=0} = Q_x|_{u=0} = 0. \end{cases} \tag{3.16}$$

Based on the boundary conditions, the expressions for each parameter can be derived as follows:

$$\begin{cases} B_1 = -K_1K_2/K_3, \qquad B_2 = K_4B_1, \qquad B_3 = K_5B_4, \qquad B_4 = K_6B_1 + K_1, \\ K_1 = -K/\left[K_3\cosh\left(\eta\dfrac{a}{b}\right)\sin\left(\xi\dfrac{a}{b}\right) + \sinh\left(\eta\dfrac{a}{b}\right)\cos\left(\xi\dfrac{a}{b}\right)\right], \\ K_2 = K_3\eta\sinh\left(\eta\dfrac{a}{b}\right)\sin\left(\xi\dfrac{a}{b}\right) + K_3\xi\cosh\left(\eta\dfrac{a}{b}\right)\cos\left(\xi\dfrac{a}{b}\right) \\ \qquad + \eta\cosh\left(\eta\dfrac{a}{b}\right)\cos\left(\xi\dfrac{a}{b}\right) - \xi\sinh\left(\eta\dfrac{a}{b}\right)\sin\left(\xi\dfrac{a}{b}\right), \\ K_3 = \eta\sinh\left(\eta\dfrac{a}{b}\right)\cos\left(\xi\dfrac{a}{b}\right) - \xi\cosh\left(\eta\dfrac{a}{b}\right)\sin\left(\xi\dfrac{a}{b}\right) + K_2\eta\cosh\left(\eta\dfrac{a}{b}\right)\sin\left(\xi\dfrac{a}{b}\right) \\ \qquad + K_2\xi\sinh\left(\eta\dfrac{a}{b}\right)\cos\left(\xi\dfrac{a}{b}\right) + K_3K_4\eta\sinh\left(\eta\dfrac{a}{b}\right)\sin\left(\xi\dfrac{a}{b}\right) \\ \qquad + K_3K_4\xi\cosh\left(\eta\dfrac{a}{b}\right)\cos\left(\xi\dfrac{a}{b}\right) + K_4\eta\cosh\left(\eta\dfrac{a}{b}\right)\cos\left(\xi\dfrac{a}{b}\right) \\ \qquad - K_4\xi\sinh\left(\eta\dfrac{a}{b}\right)\sin\left(\xi\dfrac{a}{b}\right), \\ K_4 = \left(\xi^2 - \eta^2\right)/2\eta\xi, \\ K_5 = \left(3\eta\xi^2 - \eta^3\right)/\left(3\eta^2\xi - \xi^3\right), \\ K_6 = -\left[\cosh\left(\eta\dfrac{a}{b}\right)\cos\left(\xi\dfrac{a}{b}\right) + K_2\sinh\left(\eta\dfrac{a}{b}\right)\sin\left(\xi\dfrac{a}{b}\right)\right] \Big/ \\ \qquad\qquad \left[K_3\cosh\left(\eta\dfrac{a}{b}\right)\sin\left(\xi\dfrac{a}{b}\right) + \sinh\left(\eta\dfrac{a}{b}\right)\cos\left(\xi\dfrac{a}{b}\right)\right]. \end{cases} \tag{3.17}$$

3.3. Stress distribution in the main roof

According to plate theory (Xu, 2006), the deflection functions of the main roof (Eqs. (3.11) and (3.14)) yield:

$$\begin{cases} \sigma_x = -\dfrac{Ez}{1-\mu^2}\left[\dfrac{\partial^2\omega}{\partial u^2} + \mu\dfrac{1}{\sin^2\alpha}\left(\dfrac{\partial^2\omega}{\partial u^2}\cos^2\alpha - 2\dfrac{\partial^2\omega}{\partial u\partial v}\cos\alpha + \dfrac{\partial^2\omega}{\partial v^2}\right)\right], \\ \sigma_y = -\dfrac{Ez}{1-\mu^2}\left[\dfrac{1}{\sin^2\alpha}\left(\dfrac{\partial^2\omega}{\partial u^2}\cos^2\alpha - 2\dfrac{\partial^2\omega}{\partial u\partial v}\cos\alpha + \dfrac{\partial^2\omega}{\partial v^2}\right) + \mu\dfrac{\partial^2\omega}{\partial u^2}\right], \\ \tau_{xy} = -\dfrac{Ez}{1+\mu}\dfrac{1}{\sin\alpha}\left(\dfrac{\partial^2\omega}{\partial u\partial v} - \dfrac{\partial^2\omega}{\partial u^2}\cos\alpha\right). \end{cases} \tag{3.18}$$

The expression for the maximum principal stress is as follows:

$$\sigma_1 = \frac{1}{2}\left[\sigma_x + \sigma_y + \sqrt{(\sigma_x - \sigma_y)^2 + 4\tau_{xy}^2}\right]. \tag{3.19}$$

The failure criterion for the roof is defined as follows:

$$\sigma_1 > \sigma_t. \tag{3.20}$$

In this equation, σ_t represents the tensile strength of the roof rock mass.

3.4. Analysis of main roof stress distribution

Taking the 1044 working face of the Taoyuan Mine as an example, the working face length is $b = 165\,\text{m}$, and the main roof is composed of fine sandstone. For the convenience of parameter analysis, the mechanical properties of the basic roof are assumed to be homogeneous. The rock layer elastic modulus is $E = 8\,\text{GPa}$, $\mu = 0.23$, $h = 3.9\,\text{m}$, $\sigma_t = 6.4\,\text{MPa}$, and $\theta = 42°$. The pseudo-inclination angle is taken as $\beta = 6°$ for the analysis.

Figure 4 illustrates the stress distribution patterns during the initial fracture stage. The stress distribution exhibits an asymmetrical pattern, with the maximum tensile stress of 9.08 MPa occurring at the center of the lower surface. This indicates that fracturing of the lower surface will initiate at the central region. In contrast, the edges of the lower surface are primarily subjected to compressive stress, with a maximum value of 4.25 MPa. The maximum tensile stress of 18.32 MPa occurs in the central region of the long edge on the upper surface of the main roof. The stress on the upper surface is greater than that on the lower surface, indicating that the initial fracture occurs first in the central region of the long edge on the upper surface.

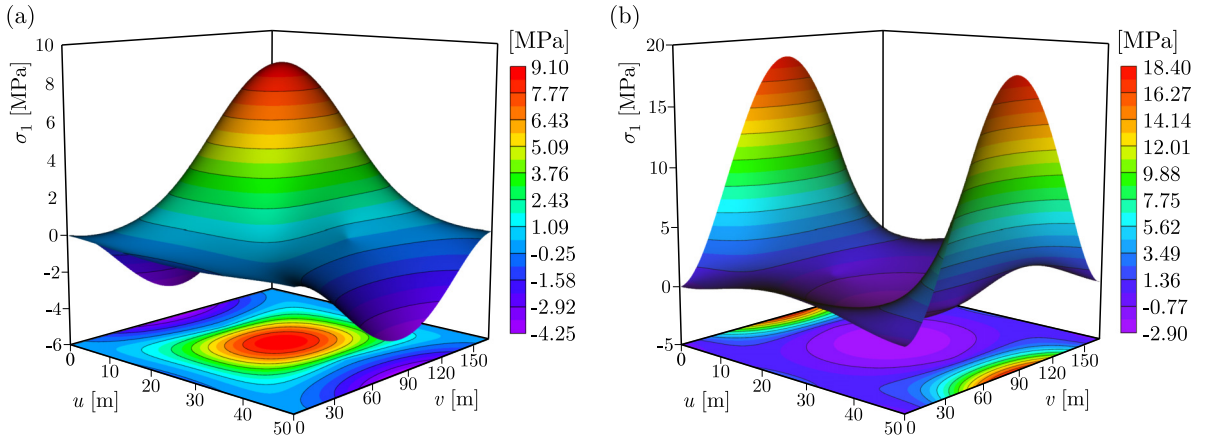

Fig. 4. Stress distribution during the initial failure of the main roof: (a) lower surface; (b) upper surface.

Figure 5 depicts the stress distribution on the upper and lower surfaces of the main roof during the periodic fracture stage. The maximum tensile stress of 2.16 MPa occurs slightly above the center of the free edge on the lower surface, which may be attributed to the linearly distributed overlying load and the parallelogram-shaped roof structure resulting from the inclined mining layout. This configuration leads to an uneven stress distribution. The maximum stress on the fixed long edge of the upper surface of the main roof is 18.74 MPa, occurring at the central region, which is greater than the maximum tensile stress on the lower surface. This indicates that the periodic fracture of the main roof first occurs in the central region of the fixed long edge on the upper surface.

3.5. Analysis of the optimal pseudo-inclined angle

In steeply inclined coal seams, a pseudo-inclined layout is commonly adopted to prevent coal self-flow and the safety hazards associated with flying debris. Therefore, determining the optimal

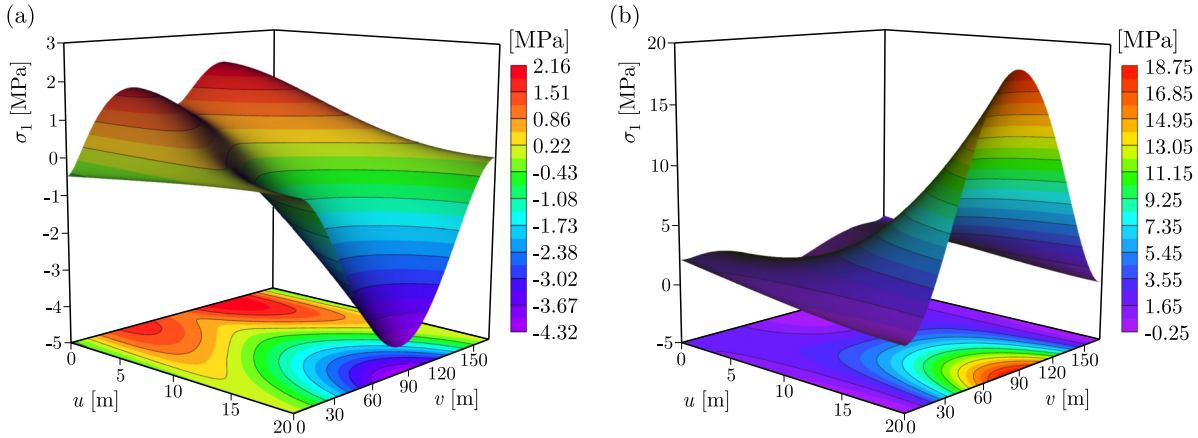

Fig. 5. Stress distribution during the periodic failure of the main roof: (a) lower surface; (b) upper surface.

pseudo-inclination angle is a critical issue. Figures 6 and 7 illustrate variations in the maximum principal stress at the main roof under different pseudo-inclination angles.

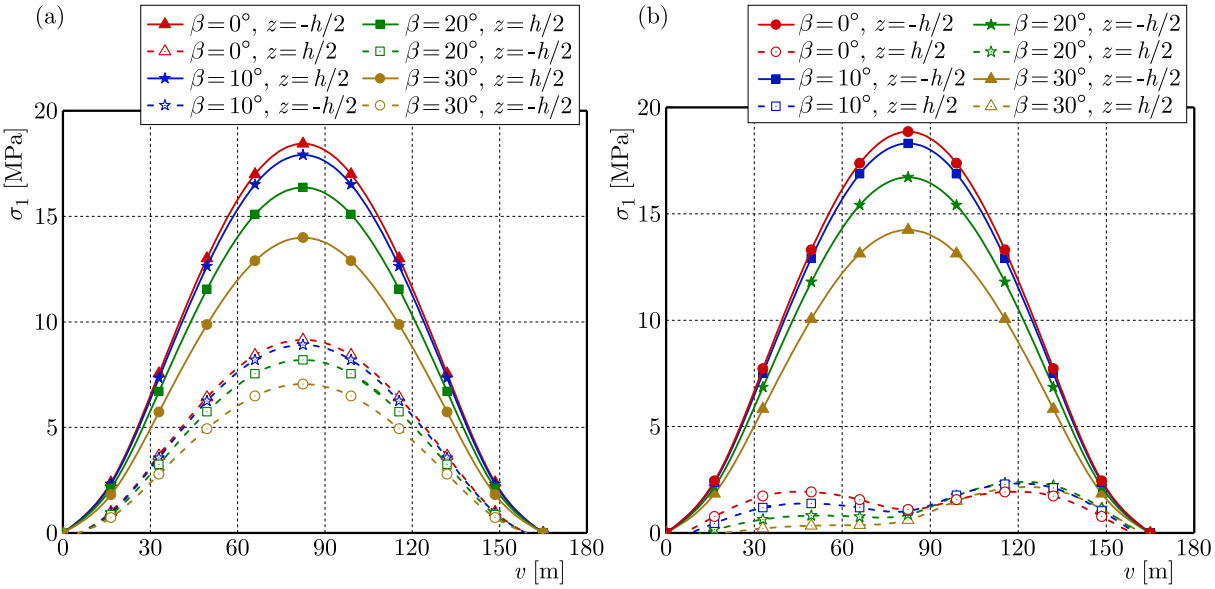

Fig. 6. Variations in deflection and maximum principal stress during initial fracture.

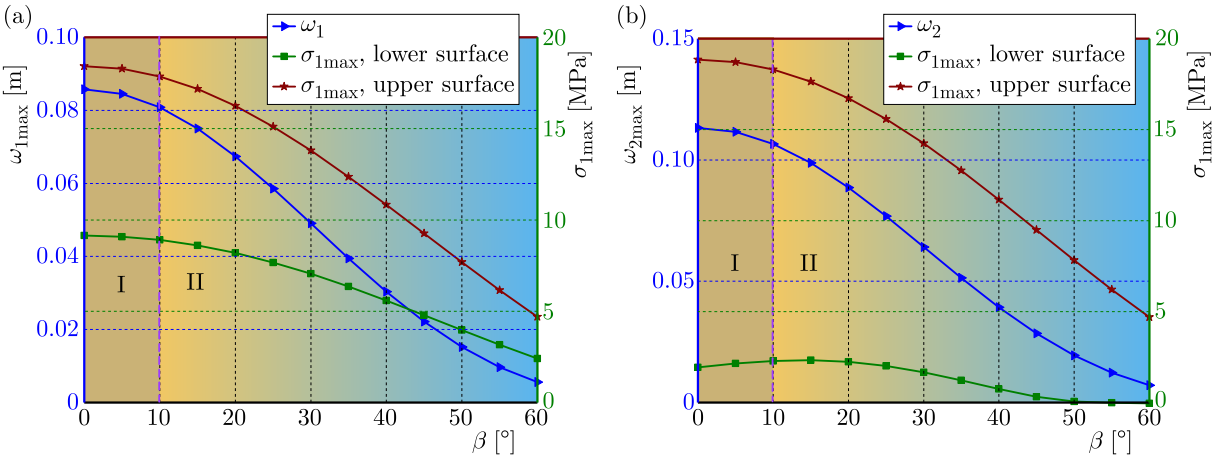

Fig. 7. Variation curves of maximum deflection and maximum principal stress with pseudo-inclination angle.

Figure 6 illustrates the variation patterns of the maximum principal stress during the initial fracture stage. As illustrated in Fig. 6a, the maximum principal stress during the initial fracture stage decreases gradually as the pseudo-inclination angle increases, thereby resulting in an extended initial weighting step distance. This is due to the fact that as the pseudo-inclined angle increases, the long edge of the roof becomes progressively larger, enhancing the support constraints along this direction, and thereby increasing the roof stability. Figure 6b illustrates the variation patterns of the maximum principal stress during the periodic fracture stage. Figure 6b indicates that the stress on the fixed boundary of the upper surface ($u = a$, $z = -h/2$) decreases as the pseudo-inclination angle increases, as is the case with the stress variation observed in the initial fracture stage. In contrast, the maximum principal stress on the free edge of the lower surface ($u = 0$, $z = h/2$) exhibits an irregular M-shaped distribution, with an increasing trend as the pseudo-inclination angle grows. The stress in the upper-middle section of the working face tends to increase, whereas the stress in the lower-middle section decreases, leading to the initial fracture of the lower surface in the upper-middle region. Because the load on the lower part of the roof is greater than that on the upper part, the fractured roof rock blocks rotate downward from the upper-middle region, posing challenges to the support of hydraulic props in the lower-middle section of the working face and the stability of the coal wall.

Figure 7 illustrates the variation curves of the maximum deflection and maximum tensile stress of the roof with respect to the pseudo-inclination angle. As the pseudo-inclined angle increases, both the deflection and the maximum principal stress decrease. As shown in region I of Fig. 7, when the pseudo-inclined angle is between 0° and 10°, the changes in both deflection and stress are relatively gradual. In region II of Fig. 7, when the pseudo-inclined angle ranges from 10° to 60°, the maximum deflection and the maximum principal stress decrease sharply, and the step distance for roof fracture also increases. Based on the above analysis, when the pseudo-inclination angle of the working face exceeds 10°, the stress distribution of the basic roof becomes significantly more uneven. This increased heterogeneity poses challenges to the hydraulic supports in the middle and lower sections of the working face and compromises coal wall stability, making roof control more difficult. Consequently, mechanized mining may face issues with equipment stability and safety. Considering these factors, the maximum pseudo-inclination angle for the 1044 working face layout should not exceed 10°.

In summary, when designing the pseudo-inclined angle for the working face, it is essential to ensure an angle that provides sufficient advance distance, thereby preventing the sliding of coal or rock that may pose a safety risk to personnel and equipment. However, during the cyclical fracture of the main roof, excessively large pseudo-inclined angles may pose challenges for hydraulic support and compromise the stability of the coal wall. Therefore, the reasonable design range of the pseudo-inclination angle of the 1044 working face is 5° to 10°, the leading distance of the working face is 14.3 m to 28.6 m. While mining the working face, the pseudo-inclination angle is set to about 8°. According to theoretical calculations, the initial fracture step distance of the main roof is 32 m, and the periodic fracture step distance is 13 m.

4. Engineering analysis

The 1044 working face utilizes a pseudo-inclined layout, with the pseudo-inclined angle controlled between 5° and 10° during mining. The hydraulic supports used on the working face are of the ZZ10000/21/45D model, with a total of 110 units, spaced at 1.5 m intervals. Pressure sensors are installed on the support units to monitor the mining pressure. A sensor is installed for every 10 sets of electromagnetic valves. The monitoring of support loads serves as a fundamental technique for assessing the stability of the working face, providing key information on roof structure evolution and the response of the support system. The layout of the working resistance measurement zones for the hydraulic supports, shown in Fig. 8a, divides the working face into five areas: lower, lower-middle, middle, upper-middle, and upper. By analyzing variations in

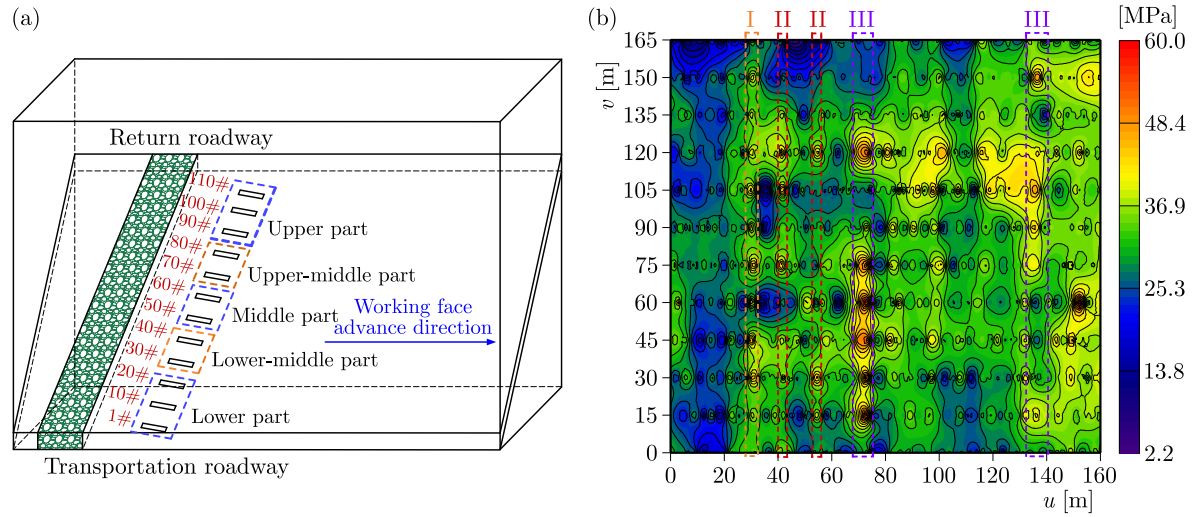

Fig. 8. Monitoring of hydraulic support load.

hydraulic support pressure, the roof fracture pattern and the collapse step distance can be determined. Based on the data obtained from hydraulic support monitoring, pressure distribution contour maps were generated using Origin software. The load distribution of hydraulic supports at different mining distances is shown in Fig. 8b.

In the load distribution map, area I represents the initial roof pressure, area II represents the periodic roof pressure, and area III shows a significant increase in support load compared to other locations, indicating roof pressure caused by the fracture of the key strata above the working face. The initial roof pressure occurs at around 30 meters, the first periodic roof pressure occurs at around 42 meters, and key strata fractures in the roof occur at 72 meters and 136 meters. During the periodic roof pressure phase, the loads on the upper and lower hydraulic supports are noticeably smaller than those in other areas. The reduced load on the upper hydraulic supports is due to the uneven distribution of the roof load, with the upper part of the roof carrying significantly less load than the lower part. The reduced load on the lower hydraulic supports may be due to two reasons: first, the pseudo-inclined mining layout results in a sharp angle at the bottom of the roof, where the constraints of the coal and overlying rock layers are stronger. Second, after the overlying strata fracture, the rock fragments slide downward, filling the lower goaf and counteracting some of the vertical stress on the roof, which slows the roof's fracture and rotation.

The support load curves for five positions on the working face: upper, upper-middle, middle, lower-middle, and lower, are shown in Fig. 9. From the variation in hydraulic support pressure at different locations, it can be observed that the initial roof pressure occurs at around 30 meters. The maximum average load during the initial roof pressure phase is 32.9 MPa, with the load at the middle of the working face exceeding that at other locations. The 50# support at the center of the working face experiences the first roof pressure at the earliest, with a maximum load of 47.3 MPa. Since the middle of the roof experiences the greatest deflection, the first fracture occurs in the middle, which is consistent with the field results and theoretical analysis.

The step distance for periodic roof pressure is 10 to 15 meters, and the first periodic roof pressure has a maximum load of 49.1 MPa, occurring at the 80# support in the middle-upper section, as shown in Fig. 9e. From the curve, it can be seen that the load at the first periodic roof pressure on the middle-upper supports is greater than the initial roof pressure, unlike the roof pressure behavior at other locations. The maximum average load during the periodic roof pressure phase is 36.9 MPa, and the load on the middle-upper section is significantly higher than that at other locations. The theoretical analysis indicates that when a pseudo-inclined layout is used, periodic fractures in the roof first occur in the middle-upper section, which

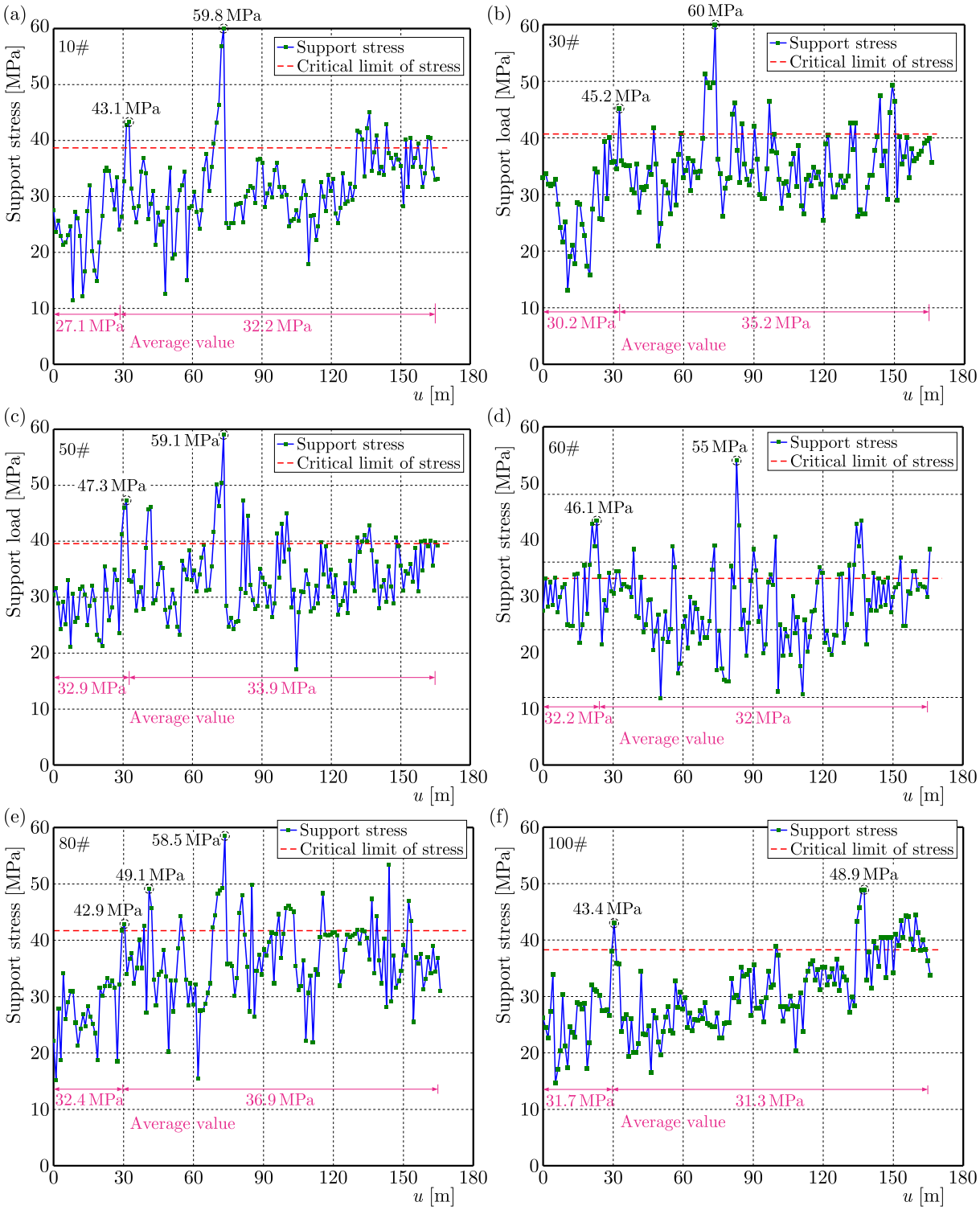

Fig. 9. Hydraulic support working resistance.

results in higher periodic roof pressure in this area. The field monitoring results confirm the reliability of the theoretical analysis. The ultimate working resistance of the hydraulic supports is 70 MPa. When the support load exceeds this limit, the support system may become overloaded, potentially compromising the stability of the mining space. Field monitoring results indicate that the peak loads during roof failure did not exceed the ultimate working resistance of the hydraulic supports. No support collapses occurred, and no large-scale coal wall spalling was observed, demonstrating that the hydraulic supports effectively maintained working face stability.

5. Discussion

This study establishes a mechanical model for the basic roof failure of pseudo-inclined working faces in steeply inclined coal seams based on elastic thin-plate theory and validates it through field monitoring. Compared with conventional roof-breakage theories that assume a rectangular plate, the present work introduces a parallelogram-plate model that better represents the spatial geometry after pseudo-inclined layout. This approach improves the applicability for simulating asymmetric deformation, stress distribution, and roof failure locations. The results indicate that both the initial and periodic breakage of the basic roof exhibit pronounced asymmetry, with failures more likely to occur in the upper-middle region, consistent with the observed mine pressure behavior.

The theoretical derivation further quantifies the influence of pseudo-inclination angle adjustment on roof deflection, principal stresses, and breakage intervals, thereby defining a rational range of angles and enhancing the theoretical basis and generalizability of angle design. It should be noted, however, that the mechanical model adopted herein remains based on the elastic thin-plate assumption and does not account for more complex factors such as stratified rock structures, jointed weak planes, or shear-dominated failure. Future research may incorporate discrete-element methods to improve the model's completeness.

6. Conclusion

To investigate the fracture mechanism of the roof in an inclined mining face of a steeply dipping coal seam and determine the optimal pseudo-inclination angle for face layout, a mechanical model of roof fracture was established. The stress and deformation characteristics of the roof were analyzed, and the reasonable range of pseudo-inclination angles was identified. Furthermore, field monitoring data were employed to validate the theoretical model. The following conclusions were drawn:

1) A mechanical model for the initial and periodic breakage of the basic roof in pseudo-inclined working faces was developed based on elastic thin-plate theory, revealing the asymmetric deformation and stress distribution induced by the pseudo-inclined layout. The results show that initial roof breakage first occurs near the fixed long edge of the upper surface and the central region of the lower surface. Periodic breakage also exhibits strong asymmetry, appearing first at the central area of the fixed long edge on the upper surface and the upper–middle portion of the free edge on the lower surface, which differs substantially from the breakage patterns typically observed in conventional coal-seam extraction.
2) As the pseudo-inclined angle increases, the maximum tensile stress in the upper-middle region of the working face rises, whereas the maximum tensile stress in the lower region decreases, resulting in reduced roof stability and concentrated loading on the hydraulic supports, thereby increasing the risk of support adaptation failure. Theoretical analysis indicates that the optimal pseudo-inclined angle for the 1044 working face ranges from 5° to 10°, which satisfies the combined requirements for equipment anti-slip performance, spontaneous gangue sliding control, and coal wall stability. Field monitoring data show that the support loads did not exceed the ultimate working resistance during extraction, and no support collapses or severe coal wall spalling occurred, confirming the rationality of the design parameters.
3) Field mine-pressure monitoring reveals that initial weighting is concentrated in the middle of the working face, while peak periodic loading occurs in the upper–middle region. These observations are fully consistent with the theoretical predictions, demonstrating that the proposed model effectively identifies roof-breakage locations and the intensity of mine-pressure manifestation in pseudo-inclined working faces. The findings provide a theoretical basis for evaluating roof stability and designing support parameters for hydraulic supports.

Acknowledgments

This research was financially supported by the National Natural Science Foundation of China (no. 52204114), the Natural Science Foundation of Jiangsu Province (no. BK20210522).

References

1. Çelik, A., & Özçelik, Y. (2023). Investigation of the effect of caving height on the efficiency of the longwall top coal caving production method applied in inclined and thick coal seams by physical modeling. *International Journal of Rock Mechanics and Mining Sciences*, *162*, Article 105304. https://doi.org/10.1016/j.ijrmms.2022.105304
2. Das, A.J., Mandal, P.K., Bhattacharjee, R., Tiwari, S., Kushwaha, A., & Roy, L.B. (2017). Evaluation of stability of underground workings for exploitation of an inclined coal seam by the ubiquitous joint model. *International Journal of Rock Mechanics and Mining Sciences*, *93*, 101–114. https://doi.org/10.1016/j.ijrmms.2017.01.012
3. Das, A.J., Paul, P.S., Mandal, P.K., Kumar, R., & Tewari, S. (2021). Investigation of failure mechanism of inclined coal pillars: Numerical modelling and tensorial statistical analysis with field validations. *Rock Mechanics and Rock Engineering*, *54*(6), 3263–3289. https://doi.org/10.1007/s00603-021-02456-5
4. Do, T.N., Wu, J.-H., & Lin, H.-M. (2017). Investigation of sloped surface subsidence during inclined seam extraction in a jointed rock mass using discontinuous deformation analysis. *International Journal of Geomechanics*, *17*(8). https://doi.org/10.1061/(ASCE)GM.1943-5622.0000894
5. Eremin, M., Peryshkin, A., Esterhuizen, G., Pavlova, L., & Fryanov, V. (2022). Numerical analysis of pillar stability in longwall mining of two adjacent panels of an inclined coal seam. *Applied Sciences*, *12*(21), Article 11028. https://doi.org/10.3390/app122111028
6. Islavath, S.R. (2023). Numerical modelling approach for estimation of a yield zone in the face of a deep longwall panel. *Scientific Reports*, *13*, Article 20811. https://doi.org/10.1038/s41598-023-47683-8
7. Islavath, S.R., Deb, D., & Kumar, H. (2016). Numerical analysis of a longwall mining cycle and development of a composite longwall index. *International Journal of Rock Mechanics and Mining Sciences*, *89*, 43–54. https://doi.org/10.1016/j.ijrmms.2016.08.003
8. Kumar, R., Mandal, P.K., Ghosh, N., Das, A.J., & Banerjee, G. (2023). Design of stable parallelepiped coal pillars considering geotechnical uncertainties. *Rock Mechanics and Rock Engineering*, *56*(9), 6581–6602. https://doi.org/10.1007/s00603-023-03415-y
9. Lang, D., Wu, X., Wu, Y., Lin, H., & Luo, S. (2021). Boundary distribution of top-coal limit-equilibrium zone in fully mechanized caving in steeply dipping coal seams. *Geomatics, Natural Hazards and Risk*, *12*(1), 2561–2589. https://doi.org/10.1080/19475705.2021.1969450
10. Li, X., Wang, Z., & Zhang, J. (2017). Stability of roof structure and its control in steeply inclined coal seams. *International Journal of Mining Science and Technology*, *27*(2), 359–364. https://doi.org/10.1016/j.ijmst.2017.01.018
11. Luo, S., Wang, T., Wu, Y., Huangfu, J., & Zhao, H. (2021). Internal mechanism of asymmetric deformation and failure characteristics of the roof for longwall mining of a steeply dipping coal seam. *Archives of Mining Sciences*, *66*(1), 101–124. https://doi.org/10.24425/ams.2021.136695
12. Pan, R., Cao, S., Shen, D., Liang, J., & Liao, J. (2017). Model of the roof fracture in pitching diagonal mining panel and its field measurement (in Chinese). *Journal of Mining and Safety Engineering*, *34*(4), 637–643. https://doi.org/10.13545/j.cnki.jmse.2017.04.005
13. Proyavkin, E.T. (1993). New nontraditional technology of working thin and steep coal seams. *Ugol Ukrainy*, *3*, 2–4.
14. Rak, Z., Stasica, J., Burtan, Z., & Chlebowski, D. (2020). Technical aspects of mining rate improvement in steeply inclined coal seams: A case study. *Resources*, *9*(12), Article 138. https://doi.org/10.3390/resources9120138

15. Sun, J., Liu, X., & Ren, T. (2019). Overburden stability of an inclined backfill stope in the context of the nonlinear elastic mechanical properties of the backfill body. *Environmental Earth Sciences*, *78*(24), Article 719. https://doi.org/10.1007/s12665-019-8728-8

16. Tu, H., Tu, S., Yuan, Y., Wang, F., & Bai, Q. (2015). Present situation of fully mechanized mining technology for steeply inclined coal seams in China. *Arabian Journal of Geosciences*, *8*(7), 4485–4494. https://doi.org/10.1007/s12517-014-1546-0

17. Wang, J.-a., & Jiao, J.-l. (2016). Criteria of support stability in mining of steeply inclined thick coal seam. *International Journal of Rock Mechanics and Mining Sciences*, *82*, 22–35. https://doi.org/10.1016/j.ijrmms.2015.11.008

18. Wang, L. (1983). The Kantorovich method for the bending problem of parallelogram plates (in Chinese). *Journal of Hunan University*, (04):36–47. https://doi.org/10.19636/j.cnki.cjsm42-1250/o3.1983.03.013

19. Wu, Y., Yun, D., Xie, P., Wang, H., Lang, D., & Hu, B. (2020). Progress, practice and scientific issues in steeply dipping coal seams fully-mechanized mining (in Chinese). *Journal of China Coal Society*, *45*(1), 24–34. https://doi.org/10.13225/j.cnki.jccs.YG19.0494

20. Xie, P., Luo, Y., Wu, Y., Gao, X., Luo, S., & Zeng, Y. (2020). Roof deformation associated with mining of two panels in steeply dipping coal seam using subsurface subsidence prediction model and physical simulation experiment. *Mining Metallurgy & Exploration*, *37*(2), 581–591. https://doi.org/10.1007/s42461-019-00156-x

21. Xu, Z. (2006). *Elasticity mechanics* (in Chinese). Higher Education Press, Beijing.

22. Yang, Y., Lai, X., Shan, P., & Cui, F. (2020). Comprehensive analysis of dynamic instability characteristics of steeply inclined coal-rock mass. *Arabian Journal of Geosciences*, *13*(6), Article 241. https://doi.org/10.1007/s12517-020-5217-z

23. Zhang, P., Li, Z., Wei, Y., Chen, Y., & Dong, L. (2025). Analysis of the roof damage range in close-proximity gently inclined coal seams mining and the feasibility of upward mining. *Scientific Reports*, *15*, Article 5324. https://doi.org/10.1038/s41598-025-89808-1

24. Zhao, Z., Pan, W., & Deng, C. (2025). Analysis of longwall shield operation in inclined coal seams. *Mining, Metallurgy & Exploration*, *42*(4), 2237–2252. https://doi.org/10.1007/s42461-025-01303-3

Manuscript received May 16, 2025; accepted for publication December 30, 2025; published online February 13, 2026.